Glass Europe Vol. 2 (2024) 1-26
https://doi.org/10.52825/glass-europe.v2i.1187

Submitted: 04 Mar. 2024 | Accepted: 08 May 2024 | Published: 03 Jun. 2024

# Phosphate/Silicate Ratio Allows for Fine-Tuning of Bioactive Glass Crystallisation and Glass-Ceramic Microstructure

Altair T. Contreras Jaimes[1,#], Gloria Kirste[1,2,#], Christian Patzig[3], Juliana Martins de Souza e Silva[3,4], Jonathan Massera[5], Natalia Karpukhina[6], Robert G. Hill[6], Araceli de Pablos-Martín[1,3,7,*], and Delia S. Brauer[1,*]

[1] Otto Schott Institute of Materials Research, Friedrich Schiller University, Jena, Germany

[2] present address: Leibniz Institute for Solid State and Materials Research, Dresden, Germany

[3] Fraunhofer Institute for Microstructure of Materials and Systems (IMWS), Halle, Germany

[4] Institute of Physics – mikroMD, Martin Luther University Halle-Wittenberg, Halle, Germany

[5] Faculty of Medicine and Health Technology, Tampere University, Tampere, Finland

[6] Dental Physical Sciences, Queen Mary University of London, UK

[7] present address: Wilhelm Dyckerhoff Institut, R&D, Dyckerhoff GmbH, Wiesbaden, Germany

[#] joint first authors: Altair T. Contreras Jaimes, Gloria Kirste

*Correspondence: Delia S. Brauer, delia.brauer@uni-jena.de,
Araceli de Pablos-Martín: araceli.pablosmartin@dyckerhoff.com

**Abstract.** A combination of XRD, solid-state NMR and state-of-the-art imaging techniques were used to investigate how the calcium orthophosphate/calcium silicate ratio affects the crystallisation of bioactive glasses in the system $SiO_2$-$P_2O_5$-CaO-$CaF_2$. In the phosphate-free glass, xonotlite, wollastonite and cuspidine crystallised. From 2.4 mol% $P_2O_5$, fluorapatite also formed, while the amount of wollastonite decreased. Crystallisation tendency was low for low phosphate contents, while above 3 mol% $P_2O_5$ it increased. The phosphate-free glass showed a volume crystallisation mechanism with constant activation energy. By contrast, the glass with the largest phosphate to silicate ratio showed both volume and surface crystallisation, causing a pronounced decrease in activation energy with crystallisation degree. This work shows that by changing the phosphate/silicate ratio we can determine which crystal phases form, obtaining for example fluorapatite-free or wollastonite-free glass-ceramics, depending on the desired application and properties such as mechanical strength or activity in contact with physiological solutions.

**Keywords:** Crystallisation, Bioactive Glass, Glass-Ceramic

## 1. Introduction

In the field of bioactive materials, glass and glass-ceramics play an important role owing to their capacity to release ions, form an apatite surface layer chemically similar to bone mineral, bond to bone and, ultimately, degrade in the body [1]. Their specific content of CaO, $Na_2O$ and $P_2O_5$ results in a glass highly degradable both *in vitro* and *in vivo*. However, due to their highly disrupted silicate network, bioactive glasses crystallise easily during annealing or sintering of scaffolds. Such uncontrolled crystallisation may negatively affect their use, as

shown for Bioglass 45S5, where crystallisation impedes viscous flow sintering and drastically lowers the mechanical properties of scaffolds [2], [3], [4].

Crystallisation may also influence ion release, apatite formation and, thus, bioactivity [5], and in various glass systems it is possible to tune these properties via crystallisation [6], [7]. Here, crystal phases and residual glassy matrix need to be taken into account as both influence glass-ceramic properties. Immersed bioactive glass-ceramics show hydroxycarbonate apatite (HCA) precipitation *in vitro*, but this is delayed compared to the parent glasses [8]. Especially the crystallisation of silicate phases delays apatite layer formation [9], [10], [11] but this is often accepted if the mechanical properties improve in parallel, like in the case of wollastonite ($CaSiO_3$) crystallisation [12]. While this delay shows a lower reactivity of the crystallised materials, it may not necessarily result in a lower *in vivo* bioactivity of the glass-ceramic, e.g. apatite/wollastonite glass-ceramics which show slower degradation *in vivo* compared to a bioactive glass but allow for improved bone ingrowth compared to other commercially used materials such as hydroxyapatite (HAp) [12], [13]. Crystallisation can have additional advantages and may, for example, be a route for preventing cytotoxicity when the release of ions is adjusted through controlled heat-treatment and crystallisation [14], [15]. The type of crystal phases present also has an effect on performance in physiological solutions, with e.g. apatite-like phases promoting apatite surface layer precipitation during immersion [6], [16], [17], [18], [19], [20], [21], in contrast to silicate phases. Crystallisation of apatite phases during heat treatment of bioactive glasses has been reported to strongly depend on the phosphate content in the glass [22].

Changes in the composition and structure of the residual glassy matrix can also affect reactions in contact with physiological solutions. If the crystal phases are enriched in modifier ions or fluoride, the silicate network polymerisation (or network connectivity [1]) of the residual glassy matrix increases and can be expected to be less reactive than the parent glass. By contrast, if the network connectivity of the residual glassy matrix remains constant, reactivity can be expected to remain constant, too. As phosphate in bioactive glasses is present as orthophosphate, charge-balanced by modifiers [23], [24], crystallisation of orthophosphate species will not affect the silicate network connectivity of the glassy matrix and, thus, is unlikely to affect the reactivity of the glassy silicate matrix.

We hypothesise that it is possible to obtain apatite crystallisation in bioactive glass-ceramics if sodium is replaced by calcium, and the calcium orthophosphate to calcium silicate ratio in the glass is increased. Incorporation of fluoride into the system is necessary, too, as hydroxyl groups are not available in a melt-derived system to allow for hydroxyapatite crystallisation. Therefore, the present work aims to investigate the crystallisation mechanism (e.g., volume or surface crystallisation) of glasses in the system $SiO_2$-$P_2O_5$-CaO-$CaF_2$ and to establish the relationship between phosphate/silicate ratio, thermal behaviour and glass-ceramic microstructure such as crystal composition, crystalline fraction, and crystal size and morphology. As the presence of apatite crystals within a bioactive glass matrix is known to influence ion release and apatite precipitation during contact with physiological solutions, this has been investigated in a separate study [25].

# 2. Experimental

## 2.1 Glass design and thermal analyses

Our aim was to vary the calcium orthophosphate to calcium silicate ratio in bioactive glasses, starting from a phosphate-free composition. If $P_2O_5$ is added to a bioactive glass without adding stoichiometric amounts of modifier oxides to allow for charge-balancing of $PO_4^{3-}$ groups, the network connectivity [1] (NC) of the silicate network increases, diminishing the bioactivity at high phosphate content [26], [27]. For this reason, $P_2O_5$ was added together

with stoichiometric CaO (i.e. added as calcium orthophosphate), thereby maintaining silicate network polymerisation and network connectivity at 2.11 (Table 1) while increasing the phosphate/silicate ratio. Glasses here also contain fluoride (as calcium fluoride) to allow for crystallisation of fluorapatite as an apatite crystal phase [28]. (Details on network connectivity in this system are given in our previous publication [25].)

The glasses were melted in a platinum-rhodium crucible; 150 g batches prepared from analytical grades of $SiO_2$ (99.0% Carl Roth, Germany), $Ca(H_2PO_4)_2{\cdot}2H_2O$ (Chemische Fabrik Budenheim KG, Germany), $CaF_2$ (Chemiewerk Nünchritz, Germany) and $CaCO_3$ (≥ 99.0% Merck, Germany). Raw materials were melted in air in an induction-heated furnace (in-house construction) at temperatures of up to 1550°C and held at the maximum temperature for 20 to 30 minutes. Glasses P0 to P3 were cast into a brass mould, surface-quenched with a copper stamp and annealed at about 670°C for 2 hours. Glasses P4 and P5 had a pronounced tendency to devitrify during cooling; therefore, these were quenched without subsequent annealing. After melting, glasses looked clear with some small bubbles present. To obtain powders, glasses were crushed with a metallic mortar, sieved (125 – 250 µm) and stored in a desiccator until further use. Glasses were named according to their $P_2O_5$ content (P0 to P5; Table 1), which varied between 0 and 5.1 mol%.

Glass transition ($T_g$; determined as the inflection point), crystallisation peak ($T_x$ onset of the first exothermic peak; $T_{c1}$ first crystallisation peak; $T_{c2}$ second crystallisation peak temperature) and melting temperature ($T_m$; determined as tangent line intersections of the offset of the endothermic signal) were determined using differential scanning calorimetry (DSC; STA 449 F1 Jupiter, Netzsch Gerätebau, Germany). 30.0±0.3 mg powder (125-250 µm) was analysed in platinum crucibles in an $N_2$ atmosphere (flow rate 20 mL/min; purity 99.9%) at heating rates of 5, 10, 15 or 20 K $min^{-1}$. For comparison, a blank run was carried out by measuring a sample-free empty crucible.

## 2.2 Glass-ceramic preparation

Glass-ceramics were prepared by heat treating the glass powders at their respective first crystallisation peak temperature (Table 1) for 1 h in air (Nabertherm P330, Germany). The samples were placed in the furnace once the required temperature was reached, kept for one hour before being taken out and air quenched at room temperature. These glass-ceramic samples were crushed and sieved again to 125-250 µm. Glass-ceramics were named according to their $P_2O_5$ content and their heat treatment temperature ($T_{c1}$; Table 1).

Additionally, bulk samples of glass-ceramics P0-846, P2-870 (obtained at the maximum temperature of a shoulder appearing at 870°C in the P2 DSC curve, interpreted as $T_{c1}$) and P2-901 (obtained at the crystallisation peak at 901°C, interpreted as $T_{c2}$) were prepared from the corresponding bulk glasses cut into 5 x 5 x 5 $mm^3$ pieces by heat treating as described for the powders.

## 2.3 X-ray diffraction and infrared spectroscopy

Crystal phases were characterised by X-ray diffraction (XRD; Rigaku Miniflex 300; Cu Kα, 15 kV and 40 mA). Patterns were recorded with a scan range between 10 and 60°2θ, a 0.01° step size and 1°/min scan speed. Full pattern analysis was carried out with MAUD software version 2.93 and Crystallography Open Database (COD) phase identification cards of cuspidine (#9014740), wollastonite (#9005777), xonotlite (#9009724) and fluorapatite (#2104744).

Attenuated total reflectance Fourier-transformed infrared spectroscopy (ATR-FTIR with diamond crystal, Cary 630, Agilent Technologies, USA) was used to examine the glass-ceramic powders in absorbance mode. Spectra were collected between 4000 and 400 $cm^{-1}$

with a resolution of 4 $cm^{-1}$ and 16 scans per measurement. An initial background scan was carried out before each set of samples.

## 2.4 Magic angle spinning nuclear magnetic resonance spectroscopy

$^{31}P$ and $^{19}F$ magic angle spinning nuclear magnetic resonance (MAS NMR) was carried out on a Bruker Avance NEO 600 spectrometer (Bruker, Germany) operating at 14.1 T magnetic field, and data acquisition and processing was carried out using TopSpin software. A standard double resonance Bruker probe with low fluorine background was used. Glass-ceramics powders were packed into a 2.5 mm rotor and rotated at 12 kHz and 22 kHz for $^{31}P$ and $^{19}F$, respectively, with 16 and 32 scans per analysis correspondingly. A single pulse sequence was used for both nuclei with a recycle delay of 60 s and 30 s for $^{31}P$ and $^{19}F$. Referencing of the $^{19}F$ chemical shift scale was performed using a secondary reference of 1 M aqueous solution of NaF, which generated a sharp signal at -120 ppm relative to the primary reference of $CF_3Cl$. [29] $^{31}P$ spectra were referenced using the primary reference of 85% $H_3PO_4$ solution.

## 2.5 Optical microscopy

*In situ* high temperature optical microscopy was carried out on polished samples of glass P0 (~12 $mm^2$ surface, 1.5 mm height) using a heated microscope stage (TS 1500, Linkam Instruments Ltd., UK) connected to an AXIO Imager Z1m microscope (Zeiss, Germany). Video imaging was processed using ZEN imaging software (Zeiss GmbH, Germany). The set-up included a heating stage containing a cylindrical ceramic chamber where the sample was placed on a 0.5 mm thick quartz disc and covered with a ceramic lid. The sample was heated through the periphery of the chamber, and slightly through the top, all being connected to a platinum heating element and a thermocouple. Glass P0 was heated at 10 K/min to 846°C in order to reproduce the conditions from glass-ceramic preparation (Section 2.2). Additionally, optical microscopy images were collected before TEM characterisation for samples P0-846, P2-870 and P2-901 bulk glass-ceramics using a Zeiss Axio Imager A1m microscope (Zeiss GmbH, Germany). Both bulk and surface of the samples were investigated.

## 2.6 Microstructural characterisation by (scanning) transmission electron microscopy

Bulk samples of P0-846, P2-870 and P2-901 were prepared for transmission electron microscopy (TEM) by wedge-polishing (Allied High Tech MultiPrep, USA). To avoid sample degradation, a water-free polishing approach was used, using propanediol as lubricant. Samples were subjected to double-sided ion-beam milling using low-energy (2.5 keV) argon ions under a small angle of incidence (6°) until grinding and polishing artefacts were removed (precision ion-polishing system, PIPS+ II, Gatan Inc.). Electron-transparent areas of the sample were selectively coated with carbon using a special coating mask prior to TEM investigation to reduce charging effects resulting from interaction with the electron beam [30].

P0-846 and P2-901 bulk TEM samples were investigated in an FEI Titan 80–300 electron microscope (Thermo Fisher Scientific Company) at 80 kV and 300 kV acceleration voltage. High-angle annular dark field (HAADF) images were collected in scanning TEM (STEM) mode, with camera length varying between 115 and 285 mm. STEM in combination with energy dispersive X-ray spectroscopy (EDX) analysis in the FEI Titan microscope was performed by means of a Super X-EDX detector (Thermo Fisher Scientific Company) consisting of four silicon drift detectors, thus offering a maximum collection angle of 0.7 sr. Elemental mappings of Si, P, Ca and F were obtained in order to gain information about elemental distribution with high spatial resolution. This was achieved by mapping the lateral distribution of the intensity of the X-Ray K lines of the respective elements. From EDX data, elemental quantification was

performed using the software Esprit1.9 (Bruker Company) with a Cliff-Lorimer approach. The percentage of oxygen was calculated as difference to 100%.

Additional STEM images of P2-870 were recorded using an FEI Tecnai G2 F20 microscope (Thermo Fisher Scientific Company) operating at 200 kV, with a camera length of 200 mm. Energy dispersive X-ray spectroscopy (EDX) area analyses of the K-lines of Si, P, Ca and F were recorded in the same microscope. Elemental quantification was performed using the software TIA (Thermo Fisher Scientific Company), with a Cliff-Lorimer approach.

### 2.7 X-ray nano-computed tomography

Selected specimens were subjected to X-ray nano-computed tomography (nano-CT) imaging (X-ray microscope Carl Zeiss Xradia Ultra 810 equipped with a chromium X-ray source, 5.4 keV). After running the TEM analysis on the P2-901 sample, the same TEM specimen was placed on top of a needle used as sample holder in nano-CT scanning, to image the same features observed by TEM. Absorption and phase-contrast imaging were performed. In the imaging experiments, a total of 901 projections were obtained over < 180°, a camera binning of 2 (128 nm of final voxel size) and with an exposure time of 10 and 25 s. Image reconstruction was performed by a filtered back-projection algorithm using the software XMReconstructor integrated into the Xradia 810 Ultra, and data were exported as a stack of 16-bit tiff images. ImageJ and commercial software arivis Vision4D (version 2.12.6) were used for image correction, segmentation and 3D renderings presented here.

## 3. Results and discussion

### 3.1 Thermal properties and glass stability against crystallisation

As a first approach of examining the crystallisation behaviour of the glasses, glass stability was evaluated by calculating the Hrubý parameter, $K_H$ (Eq. 1) [31], [32]. Here, $T_x$ is the onset temperature of the first exothermic (crystallisation) peak, $T_g$ is the glass transition temperature and $T_m$ the melting temperature; all obtained at 10 K min$^{-1}$ (Figure 1a).

$$K_H = \frac{(T_x - T_g)}{(T_m - T_x)} \quad (1)$$

The Hrubý parameter, and thus the stability against crystallisation, increases very slightly first from P0 to P1 and then decreases for the remaining glasses, with P5 showing the lowest value of all glasses (Figure 1). Small $P_2O_5$ additions (below 3 mol%) seem to have a relatively small effects on $K_H$, while larger additions seem to increase the crystallisation tendency of the melt. This agrees with the finding that it was difficult to obtain P5 as bulk, as the composition crystallised spontaneously.

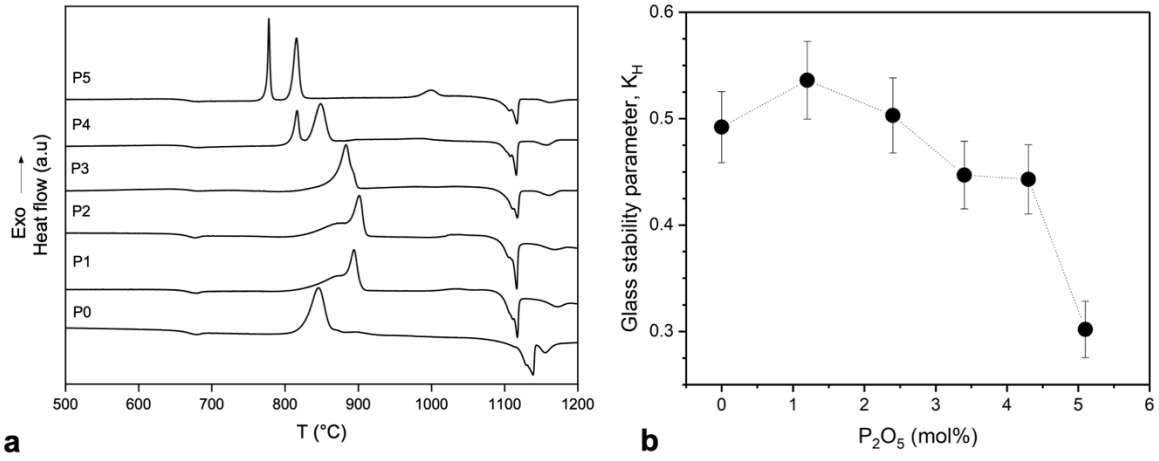


***Figure 1.*** *(a) DSC curves of the glass powders. (b) Hrubý glass stability parameter, $K_H$, of the glasses as a function of $P_2O_5$ content (dotted line acts as a visual guide only).*

$P_2O_5$ can act as a network former, which in silicate glasses is known to cause phase separation at certain concentrations. In bioactive phospho-silicate glasses, it is mostly present as orthophosphate tetrahedra (charge-balanced by modifier cations such as calcium). Computer simulations suggest that clustering and, thus, potential phase separation here occur at relatively high concentrations only [33]. We may therefore expect that in the present study, phosphate-rich regions in low phosphate content glasses (P0 to P2) did not reach critical size for crystallisation, while in the compositions with higher phosphate contents critical size of the regions or clusters may have been achieved, resulting in a more pronounced tendency to crystallise, as shown by the decreasing value for $K_H$. Phase separation was indeed observed for glasses P0, P2 and P5 as shown previously [34], and for P5 involved phosphate phases. This may affect the observed temperature behaviour of P5 and will be discussed further below.

$T_g$ values (Table 1) were similar for all glasses, reflecting the constant silicate network polymerisation (constant NC) and indicating a negligible effect of the phosphate/silicate ratio on $T_g$ in the present system. The observed $T_g$ values (around 670°C) were much higher than those reported for conventional bioactive glasses with comparable NC. For instance, glass 45S5, with its NC of 2.11, has reported $T_g$ values between 520 and 560°C [4], [35], [36]. The higher $T_g$ values observed here originate from the absence of $Na_2O$ in the glass system, which is known for lowering $T_g$ because of the lower field strength of sodium compared to calcium cations [37]. A previous study on a comparable Na-free bioactive glass (44.88 $SiO_2$, 0.97 $P_2O_5$, 44.87 CaO, 9.28 $CaF_2$, in mol%, NC 2.13) shows a similar $T_g$ value of 654°C [22], confirming the expected influence of the modifier cation field strength.

***Table 1**. Nominal compositions of the melt-derived glasses (mol%; network connectivity is 2.11) and their corresponding glass-ceramics and results of thermal analysis (error ± 5 K) of the glasses ($T_g$ glass transition temperature, $T_x$ onset of the first exothermic peak, $T_{c1}$ first crystallisation peak, $T_{c2}$ second crystallisation peak temperature, $T_m$ onset of endothermic peak corresponding to the melting temperature; all in °C).*

| Glass | $SiO_2$ | $P_2O_5$ | CaO | $CaF_2$ | $T_g$ (°C) | $T_x$ (°C) | $T_{c1}$ (°C) | $T_{c2}$ (°C) | $T_m$ (°C) | Glass-ceramic |
|---|---|---|---|---|---|---|---|---|---|---|
| P0 | 46.8 | 0.0 | 44.2 | 9.0 | 669 | 824 | 846 | | 1111 | P0-846 |
| P1 | 44.3 | 1.2 | 45.5 | 9.0 | 669 | 826 | 894 | | 1095 | P1-894 |
| P2 | 41.9 | 2.4 | 46.7 | 9.0 | 671 | 820 | 870 | 901 | 1092 | P2-901 |
| P3 | 39.9 | 3.4 | 47.7 | 9.0 | 672 | 810 | 884 | | 1100 | P3-884 |
| P4 | 38.0 | 4.3 | 48.7 | 9.0 | 670 | 807 | 815 | 848 | 1092 | P4-816 |
| P5 | 36.3 | 5.1 | 49.6 | 9.0 | 668 | 772 | 778 | 815 | 1091 | P5-778 |

$T_m$ values (Table 1) are also similar for all glasses, with the exception of glass P0 showing a higher $T_m$ than that of the other glasses. $T_m$ of glass P0 agrees well with the temperature of the four-phase intersection point between $CaF_2$, wollastonite, cuspidine and a liquid phase in the thermodynamic system $SiO_2$-CaO-$CaF_2$ [38]. A similar first melting reaction occurs for the phosphate-containing compositions, which is in good agreement with our XRD results (see below). However, the temperature of the invariant reaction is reduced by $P_2O_5$ addition.

While phosphate-free glass P0 showed only one crystallisation peak, glasses P1, P2 and P3 showed a shoulder on the left-hand side of the main crystallisation peak. This asymmetry indicates overlapping crystallisation processes of different phases, as discussed below. Glasses with an even higher phosphate/silicate ratio, P4 and P5, exhibited two well-defined crystallisation peaks (Figure 1a).

## 3.2 Structural characterisation of crystalline phases

All glass-ceramics showed complex diffraction patterns with multiple phases (Figure 2a), agreeing with the asymmetric or multiple crystallisation peaks observed in DSC traces. ATR-FTIR spectra (Figure 2b) show a superposition of broad features from the residual glassy matrix and the narrow bands of crystalline phases. Phosphate-free glass P0, shown as an example of the starting material, exhibited the characteristically broadened bands positioned between 1000 and 910 $cm^{-1}$ corresponding to Si-O-Si and Si-NBO (NBO: non-bridging oxygen) vibrations respectively [39]. Spectra of the glass-ceramics also show these broad bands, suggesting a structural similarity between glass-ceramics and corresponding parent glass, i.e. similar structural units present in a crystalline or amorphous environment. According to XRD and FTIR results, cuspidine, $Ca_4Si_2O_7F_2$, crystallised in all glass-ceramics, while wollastonite, $CaSiO_3$, was identified in samples P0-846, P1-894, P2-901 and P3-884. (A high-temperature phase of $CaSiO_3$, pseudo-wollastonite, has also been reported to crystallise during heat treatment of bioactive glasses [40] but was not detected here.) An apatite phase was present for the higher phosphate content glass-ceramics (above 3 mol%), with apatite's four highest intensity diffraction lines at about 32, 33, 26 and 50°2θ being observed in the diffraction pattern. As shown below, this phase was later identified as fluorapatite ($Ca_5(PO_4)_3F$) or a fluoride-containing apatite phase by $^{19}F$ MAS NMR spectroscopy.

The position of the diffraction lines varies slightly within the series without showing clear trends, probably due to underlying differences in lattice constants related to different substitutions and defects. In the FTIR spectra apatite was indicated by a split band positioned at approximately 600 and 570 $cm^{-1}$, associated with the P-O bend from a crystalline calcium orthophosphate phase [8] and a vibrational mode from the developing crystal phase [5], [39]. In contrast to XRD patterns, these features were already visible for P2-901 with its lower phosphate content. Xonotlite ($Ca_6Si_6O_{17}(X)_2$, X = OH, F) was identified for P0-846, P3-884, P4-816 and P5-779. Xonotlite crystallises between 750 and 800°C, and it was, together with wollastonite, the predominant phase in $SiO_2$-CaO-$CaF_2$-$K_2O$ glass-ceramics, with the ratio of the two phases depending on the fluoride content [41]. Xonotlite also formed a minor phase in canasite-type glass-ceramics up to 950°C [42]. In the present study, xonotlite was identified by small FTIR bands at approximately 650 and 1190 $cm^{-1}$, the latter being characteristic for the $Q^3$ Si-O stretch vibration of xonotlite [43]. Typically, Si–O IR bands move to higher energies, i.e. larger wavenumbers, with increasing numbers of bridging oxygen atoms (BO) connected to an $SiO_4$ tetrahedron, with $Q^3$ groups usually appearing at around 1100 $cm^{-1}$. $Q^2$ groups (present in both wollastonite and xonotlite) are expected at around 950 $cm^{-1}$ and $Q^1$ groups (in xonotlite [44] and cuspidine) at slightly below 900 $cm^{-1}$, Figure 2a [45].

Figure 2c shows the relative amounts of crystalline phases vs. phosphate content in the glass-ceramics, obtained from XRD full pattern refinement (residual glassy matrix was treated as part of the background signal). As discussed above for XRD and FTIR, an increase in phosphate/silicate ratio resulted in larger amounts of the apatite-type phase. The amounts of silicate-containing phases, i.e., cuspidine and wollastonite, show a maximum for glass-ceramic P1-894 and then decrease with increasing phosphate content, owing to less $SiO_2$ being available to form stoichiometric silica-containing phases. The decrease in the cuspidine fraction may also be related to the fluorine loss observed for high phosphate contents as shown previously [46]. As a result, $Ca_5(PO_4)_3F$ or $Ca_6Si_6O_{17}F_2$ formed instead of cuspidine ($Ca_4Si_2O_7F_2$).

Relating these tendencies to heat treatment temperature (Table 1) shows that higher temperatures promote crystallisation of silicate-containing phases, with the exception of xonotlite ($Ca_6Si_6O_{17}F_2$). As described in the literature, xonotlite is not stable at high temperatures and tends to be replaced by wollastonite [47], [48]. Parent glasses with higher phosphate/silicate ratio such as P5 have a more pronounced tendency to crystallise, as indicated by the Hrubý parameter (Figure 1). In addition to apatite crystallising at lower temperatures, an increase in phosphate content in bioactive-type glasses caused a larger number of orthophosphate units in their atomic structure which promote crystallisation [38], [49]. In addition, our previous results showed that glass P5 was phase separated and phases included phosphate phases [34]. Phase separation is a known step leading to crystallisation and may therefore contribute to the pronounced crystallisation tendency of P5.

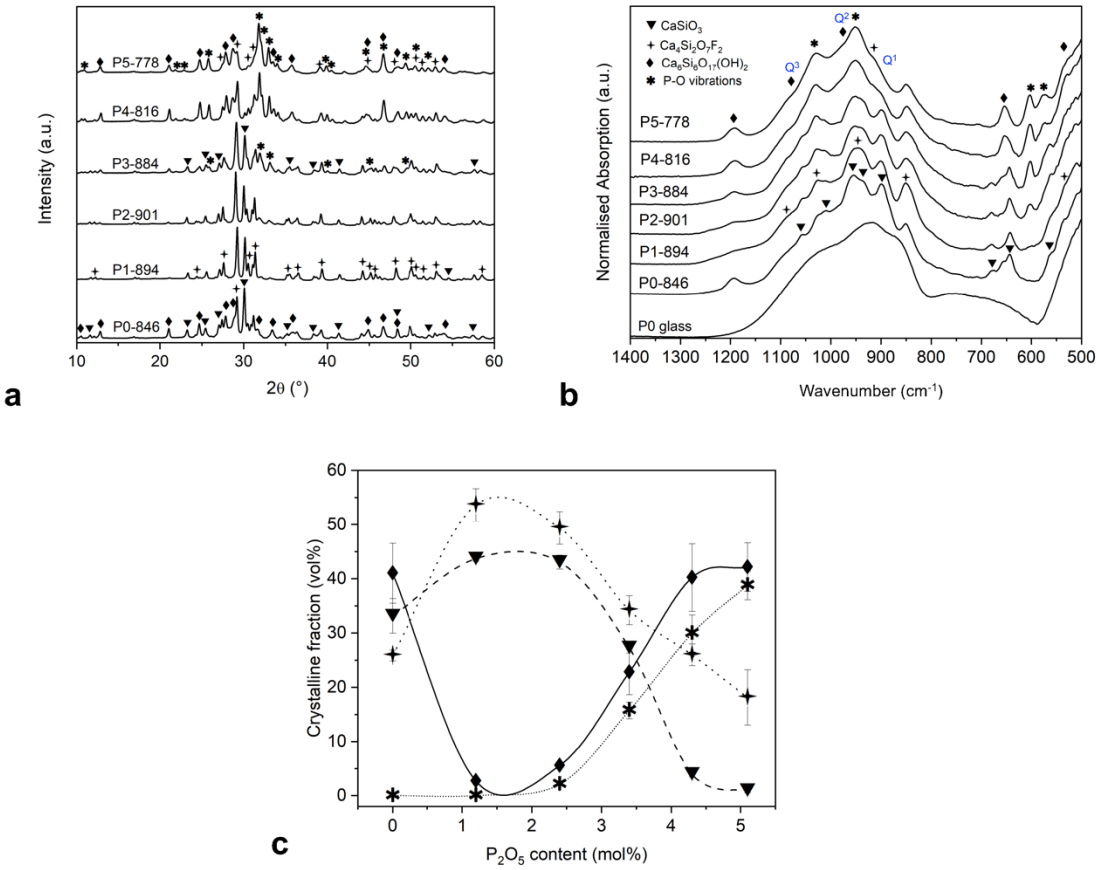


***Figure 2.*** *(a) XRD patterns and (b) FTIR spectra of glass-ceramics P0 to P5 after heat treatment for one hour at $T_{c1}$. (c) Crystalline fractions of silicate and phosphate phases from XRD full pattern refinement, plotted over the $P_2O_5$ content in the parent glass, labelled as ▼ wollastonite ($CaSiO_3$), ♦ xonotlite ($Ca_6Si_6O_{17}(OH)_2$ having been used for XRD pattern refinement, while the fluoride-containing variant, $Ca_6Si_6O_{17}F_2$, is more likely), ✦ cuspidine ($Ca_4Si_2O_7F_2$), and ✱ fluorapatite ($Ca_5(PO_4)_3F$). $Q^1$, $Q^2$ and $Q^3$ indicate the regions for bands corresponding to Si–O vibrations of $SiO_4$ tetrahedra with 1, 2 or 3 bridging oxygens, respectively, in FTIR spectra.*

Figure 3a shows the $^{31}P$ MAS-NMR spectra of selected glass-ceramics together with those of their parent glasses for comparison. In general, the peaks observed for the glass-ceramics are narrower than those of the glasses, in agreement with a larger degree of structural order. Narrow resonance bands were positioned at 2.72 ppm for P2-901 and P3-884 and at 3.22 ppm for P5-778. In crystalline materials, peaks in this region (around 2.9 ppm) have been assigned to apatite [50], [51], and we assign them to isolated orthophosphate units charge-balanced by calcium [52], [53]. XRD patterns only showed apatite above 3 mol% $P_2O_5$ (P2); however, the narrow width of the signals (compared to the orthophosphate signal from the untreated glasses) suggests crystalline calcium orthophosphate structures even for P2-901. The amount of apatite present in P2-901 may thus have been too small for detection by XRD. The signal width broadened for P5, which could be caused by the presence of nanoscale crystalline apatite structure in comparison with P2 and P3 or possibly from a mixed hydroxyfluoroapatite environment [54], [55].

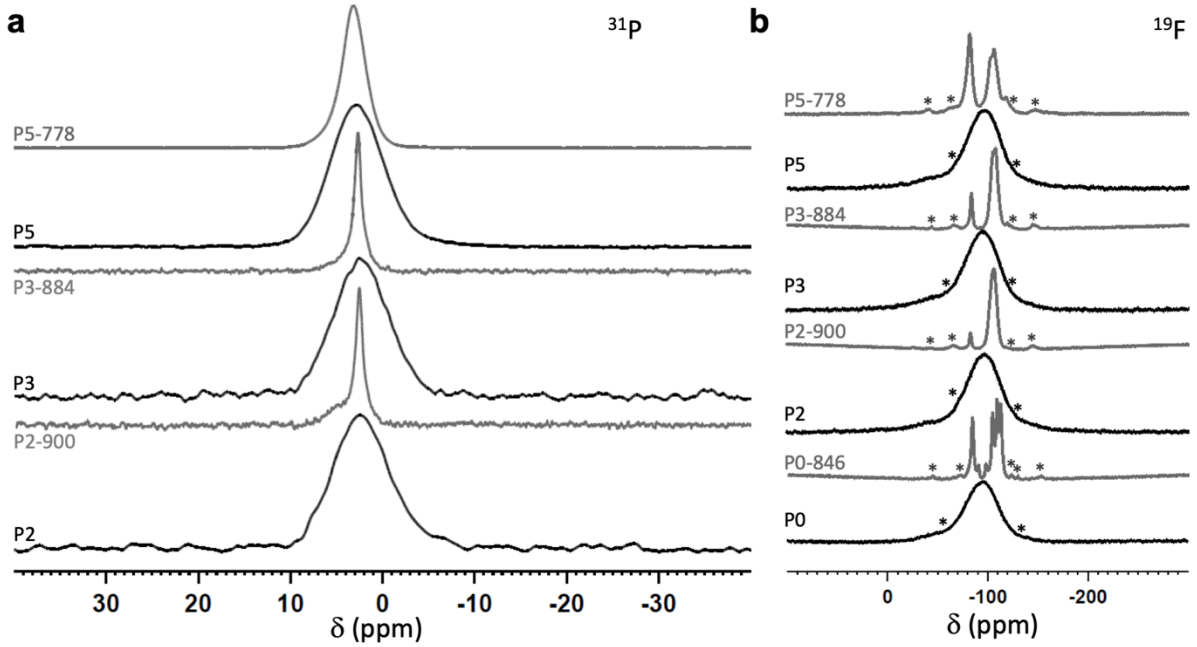


***Figure 3.*** *(a) $^{31}P$ MAS NMR and (b) $^{19}F$ MAS NMR spectra of selected glass-ceramics and their parent glasses. For chemical shifts of peaks in $^{19}F$ MAS NMR, see Table 2. The asterisks mark spinning side bands in $^{19}F$ MAS NMR spectra.*

Identification of fluorapatite is not possible by $^{31}P$ MAS NMR alone due to the structural similarities around phosphorus for different apatites [56]. Therefore, $^{19}F$ MAS NMR was used to confirm the presence of fluorapatite, and Figure 3b shows spectra and chemical shifts of selected glass-ceramics. Here, again, the resonances of the glass-ceramics are much narrower than those of the parent glasses, due to larger structural order. In the glass-ceramics a complex pattern of several partially overlapping peaks can be seen. Some of the major ones are listed in Table 2. The broad resonance between -83 and -89.2 ppm in the glass samples has been reported to correspond to an amorphous F-Ca(n) environment, where n < 3 [29], [57]. However, a much sharper $^{19}F$ signal at around -83 ppm was consistently observed in all crystalline samples, with its intensity being lowest in the P2-901 sample. This signal was preliminarily assigned to the fluorine in xonotlite based on similarity between the $^{19}F$ intensity trend with the change in fraction of xonotlite obtained from XRD, but this $^{19}F$ assignment has to be investigated further.

The chemical shift at -103 ppm is typically associated with fluorapatite in the literature [58], in agreement with our XRD data. Here, this assignment can only apply to the phosphate-containing glass-ceramics P3-884 and P5-778 and not to phosphate-free P0-846. Cuspidine has also been reported to give resonances in this region, with chemical shifts reported at -100 and -105 ppm for the pure synthetic mineral and one broad resonance at -100 ppm for slightly disordered cuspidine [59]. This may therefore explain the signals in this region observed for P0-846. The resonances at around -106.0 ppm are not easy to explain, as according to XRD no fluorite ($CaF_2$) was present in the glass-ceramics, which would give a signal in this region [60], [61]. However, It is possible for the $^{19}F$ signal of hydroxyfluoroapatite to appear at chemical shifts down to -106 ppm, and this may be the case here [55]. Resonances appearing at -111.1 and -118.9 ppm were observed in P0-846 and P5-778, respectively, and we cannot currently assign them to any of the phases identified by XRD. Taken together, the fluorine environment observed in $^{19}F$ NMR spectra is rather complex despite the apparent simplicity of the system as well as the XRD and electron microscopy results (see below), and the peak assignment will need to be investigated in more detail in the future. Besides the main peaks listed in Table 2, some of the minor intensity peaks possibly originate from a complex pattern

of sidebands (Figure 3b), which have been previously reported e.g. for a $^{19}F$ apatite study, showing eight sidebands for a single spectral component [56].

***Table 2.*** *$^{19}F$ chemical shift positions ($^{19}F$ $\delta$, in ppm) for from the NMR spectra of glass-ceramics shown in Figure 3b.*

| **Sample** | **$^{19}F$ $\delta$** | | | | | |
|---|---|---|---|---|---|---|
| P0-846 | -83.1 | -89.2 | -96.5 | -103.1 | -107.6 | -111.1 |
| P2-901 | -82.9 | - | - | - | -106.0 | - |
| P3-884 | -82.9 | - | - | -105.0 | -106.7 | -118 |
| P5-778 | -82.8 | - | - | -103.1 | -107.1 | -118.9 |

Figure 4a-c and a supplementary video (details shown below in the section *Underlying and Related Material*) show a crystallisation sequence from *in situ* high temperature optical microscopy of a bulk sample of phosphate-free glass P0, illustrating the formation and growth of crystalline species in the internal volume (volume crystallisation). The sample was heated at 10 K/min and maintained at $T_{c1}$ (846°C). An interesting phenomenon appears at approximately 90 min of treatment with two crystals growing radially to finally coalesce with other crystals to occupy the sample volume (Figure 4b).

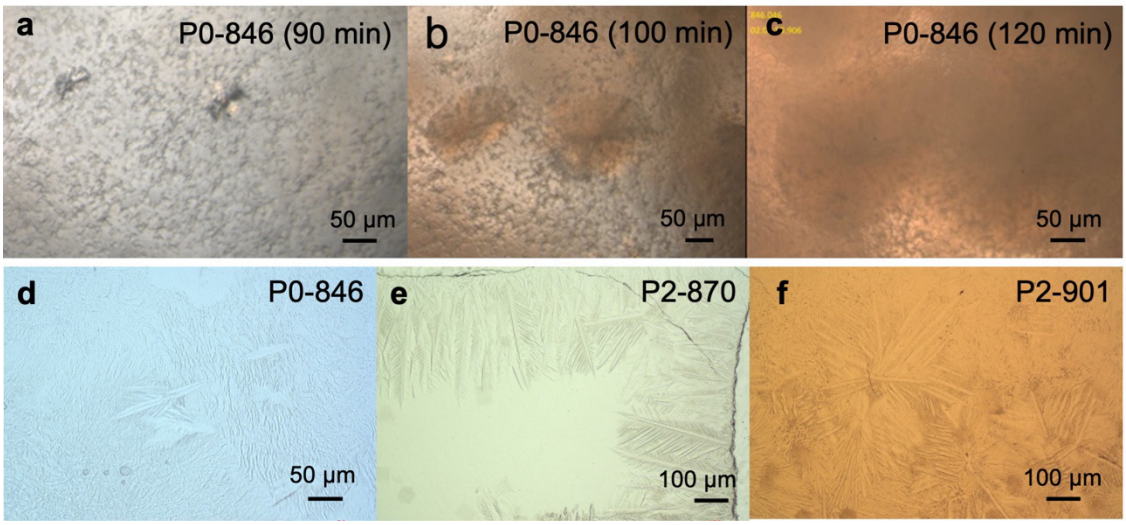


***Figure 4.*** *(a-c) In situ high temperature optical microscopy images for glass P0 heat treated for (a) 90 min, (b) 100 min and (c) 120 min, showing growth and coalescence of two crystals growing radially within the glassy matrix. (d-f) Optical microscopy images of bulk samples corresponding to glass-ceramics (d) P0-846, (e) P2-870 and (f) P2-901.*

Conventional optical microscopy of bulk glass-ceramic P0-846 (Figure 4d) showed needle-shaped features in the internal volume, with lengths of up to 100 µm. By contrast, bulk glass-ceramic P2-870 showed pine leaf-shaped structures (Figure 4e) reaching several hundreds of micrometres in length. Their growth started at the edge of the sample (surface crystallisation) and continued towards the bulk, leaving the centre free of crystals. Additional heat treatment at the second crystallisation peak temperature (P2-901) resulted in pine leaf features filling the entire volume (Figure 4f).

STEM-EDX analyses of glass-ceramics P0 and P2 only allowed for observation of a fraction of these elongated structures, as they were much larger than the TEM field of view. EDX quantification of fluorine is challenging as F-Kα X-rays have a comparably low photon energy, increasing the possibility of X-ray absorption prior to reaching the EDX detector and, as a result, underestimation of the actual fluoride content. Figure 5 shows these needles to be

depleted in silicon compared to the surrounding matrix and enriched in fluoride and calcium (Area 1, sample P0-846). Elemental quantification on one of the needles (Area 1 in Figure 5a, Table 3) gave an Si:F ratio of nearly 1:1 (assuming an underestimation of F) together with a Ca content larger than that of Si, suggesting cuspidine, $Ca_4Si_2O_7F_2$, crystallising in needle morphology. This agrees with reports on needle-like and fibrous morphology [59], [62] as well as surface crystallisation in a comparable micrometre-size range in SiO2-CaO-CaF2 glasses heat-treated at comparable temperature (899°C) [63], [64], [65].

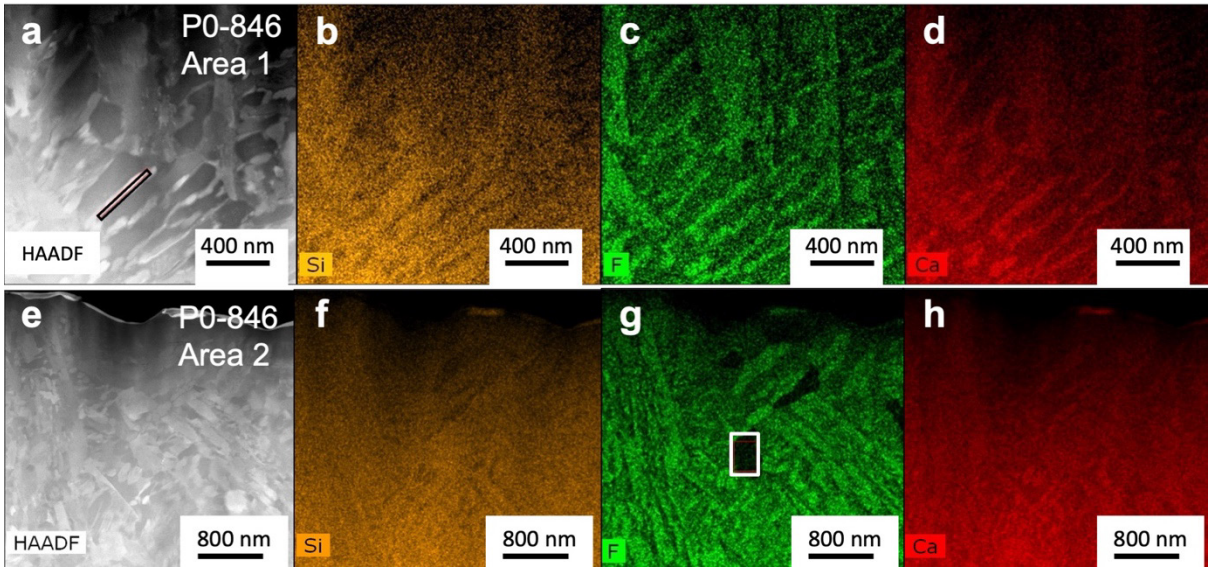


***Figure 5.*** *HAADF STEM micrographs of two areas of glass-ceramic P0-846 and corresponding EDX elemental distribution mappings: (a-d) Area 1 and (e-h) Area 2, with mappings showing Si (orange), F (green) and Ca (red). Areas 1 in (a) and 2 in (g) indicate the regions where EDX quantifications were performed (Table 3).*

In addition to the cuspidine needles, a second area of this sample (Area 2 in Figure 5g) showed irregular areas of some hundreds of micrometres depleted in fluoride, with an Si:Ca ratio of 1:1 corresponding to wollastonite ($CaSiO_3$) or xonotlite ($Ca_6Si_6O_{17}F_2$). Xonotlite has been reported to crystallise in the bulk [66], forming radiating structures [42], [47]. Lin et al. reported different microstructures for wollastonite and pseudowollastonite in bulk glasses [67], with wollastonite spherulites of ca. 50 to 100 µm in size growing in the interior of the sample. Such radial microstructures agree with the heat treatment sequence of glass P0 at 846°C shown in Figure 4a-c. Wollastonite in a rod-shape morphology also has been reported for bulk glasses [68]. Thus, based on the internal microstructure and elemental analysis observed for glass P0, we conclude that cuspidine needles form together with fluoride-depleted sub-micron grains, attributed to wollastonite and xonotlite crystals, similarly to glass-ceramics in the system $K_2O$-CaO-$SiO_2$-F where a combination of wollastonite and cuspidine formed as major phases with xonotlite as a secondary phase [62].

***Table 3.*** *Concentration of elements (at%) in bulk glass-ceramics P0-846, P2-869 and P2-901 analysed by EDX in the areas highlighted in Figures 5 and 6. The analytical accuracy of the EDX measurement was around 2%.*

| Sample | Position | Si | Ca | F | P | O |
|---|---|---|---|---|---|---|
| **P0-846** | Figure 5a, Area 1 | 19.0 | 28.9 | 13.9 | - | 38.1 |
| | Figure 5g, Area 2 | 24.5 | 25.2 | 1.4 | - | 48.9 |
| **P2-870** | Figure 6a, Area 1 | 19.0 | 29.7 | 6.6 | 1.9 | 42.9 |
| | Figure 6a, Area 2 | 22.2 | 23.0 | - | 2.0 | 52.3 |
| **P2-901** | Figure 6c, Area 1 | 21.0 | 26.0 | 4.3 | - | 48.0 |
| | Figure 6c, Area 2 | 6.6 | 29.0 | 5.5 | 11.0 | 48.0 |

Figure 6a shows a STEM micrograph of bulk glass-ceramic P2-870. A feather-shaped feature (Area 1 in Figure 6a) possibly corresponded to the needle edges shown in optical microscopy (Figure 4e), together with a smoother pore-containing feature (Area 2 in Figure 6a). An analysis of this area revealed a higher Ca than Si content and the presence of fluorine, attributed to cuspidine [62]. Quantification of elements in Area 2 (Figure 6a) matched wollastonite or xonotlite instead (Si:Ca ratio of 1:1) [42], [47], [65], [66], [67].

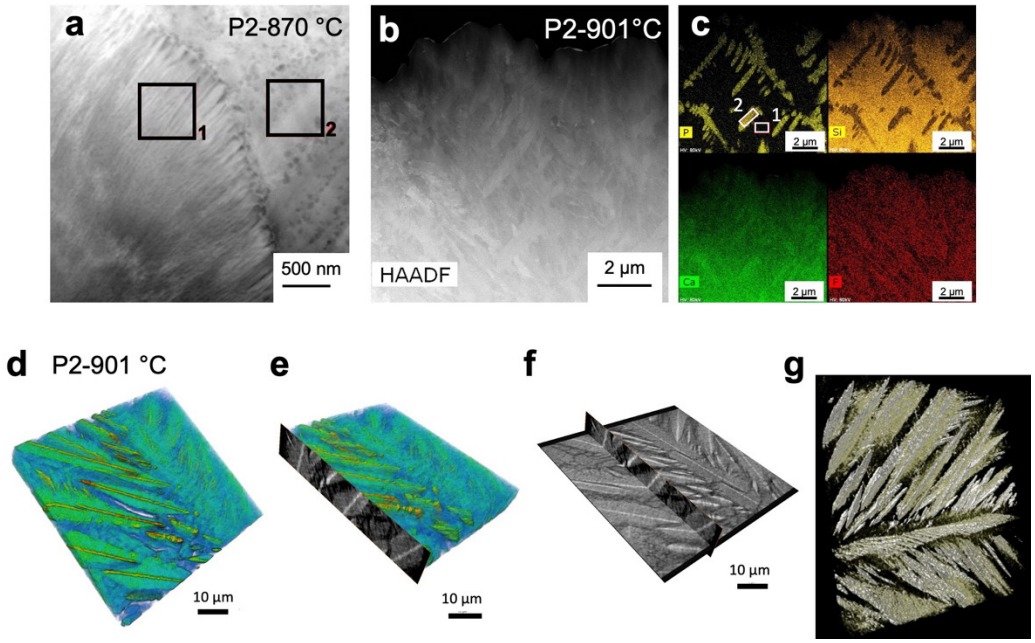


***Figure 6.*** *(a) HAADF micrograph of bulk glass-ceramic P2-870. Rectangles indicate the areas where EDX analyses were performed (Area 1 and 2 in Table 3). (b) HAADF micrograph of glass-ceramic P2-901 and (c) corresponding EDX elemental distribution mappings (P yellow, Si orange, Ca green, and F red). EDX quantification was performed in areas 1 and 2 of the P mapping. (d-g) Nano-CT images of sample P2-901 prepared for TEM, showing different virtual cuts along the volume: (g) detailed reconstruction showing the pine leaf-shaped crystals, brighter areas in the slices in (e) and (f), or pseudo-coloured in red/orange in (d) and (e) are enriched with Ca and P.*

Well-defined pine leaf-shaped crystals of some micrometres in length appeared for P2-901 (Figure 6b); elemental distribution mappings (Figure 6c) show these to differ from P2-870, being enriched in P and slightly enriched in Ca while being depleted in Si (Area 2 in Table 3). Needle-like fluorapatite has been observed in dentine and enamel [19], [20], [21], and the observed Ca:F ratio close to 5:1 agrees with fluorapatite. In this particular area, Si, Ca and F concentrations of the matrix (Area 1 in Figure 6c, Table 3) were in between those observed for wollastonite and cuspidine in P2-870, suggesting residual glassy matrix with wollastonite

and cuspidine intergrown on a nanoscale surrounding the observed fluorapatite needles in this area.

Owing to the larger field of view of nano-CT in comparison with that of TEM, pine leaf-shaped crystals (attributed to fluorapatite, Figure 6d-g) of several tens of micrometres in length could be observed. Two-dimensional plates of different sizes forming the pine leaf are discerned. Moreover, higher X-ray absorption (represented by a red colour in Figures 6d,e and as brighter areas in the slices in Figures 6e,f) was observed in the spine of the leaf-shaped structure and the thinner dendrites emerging from it. The space between the dendrites was occupied by residual glassy matrix, represented by the black colour in Figure 6e,f. Figure 6g offers a detailed view of the morphology of these crystalline structures.

The heavily intergrown morphology observed for P0-846, with most features being below the size of 1 µm, indicates bulk crystallisation rather than surface crystallisation, discussed further below. By contrast, the long, parallel calcium phosphate crystals of several tens of micrometres in length observed for P2-870 indicate growth selection by surface nucleation. Several very small crystalline phases, however, did not point at surface nucleation in agreement with the absence of very sharp reflexes in XRD.

The crystallisation of needle-like crystals may give these glass-ceramics interesting mechanical properties, as shown for comparable structures present in the $SiO_2$-$Al_2O_3$-$P_2O_5$-CaO-$CaF_2$ system [69], but this requires further investigation. Wollastonite crystallisation was also shown to enhance mechanical properties compared to glass-ceramics containing solely apatite [6], [12], [70].

## 3.3 Crystallisation mechanisms

Figure 7 displays the results of the DSC investigation on glasses P0, P4 and P5. As glasses P1, P2 and P3 exhibited very asymmetric exothermic peaks and shoulders (Figure 1a), no detailed DSC investigation was performed with these glasses. For glasses P0, P4 and P5, by contrast, detailed DSC analyses could be performed (Figure 7); however, as the glass particle size used was in the range of 125 to 250 µm, a direct comparison with microscopy results from bulk samples (Figures 4-6) was not possible. Glass P0 showed one broad crystallisation peak, while P4 and P5 each showed two narrower peaks (Figure 7a). A narrow crystallisation peak typically indicates bulk crystallisation, while a broader one suggests surface crystallisation. In addition, crystallisation peak width can give an indication of the dimensionality (surface *vs*. bulk crystallisation) of the crystals, where three dimensional crystals lead to a broader peak than needle- or plate-like crystals [71]. This agrees with the radial and irregular microstructures observed in Figures 4a-c and 5g for wollastonite/xonolite crystals, the main phases in glass-ceramic P0.

Glasses P4 and P5 each exhibited two well-defined exothermic events. The narrow shape of these peaks, less than 20 K in width, indicates that crystallisation occurred in a very narrow temperature range with the crystalline phases possessing very similar crystallisation temperatures. The peak overlap was not as pronounced as for P0, which can be seen even more clearly for the crystallisation degree curves (Figure 7b, marked in grey). Only the curves of both crystallisation peaks at 15 and 20 K/min, $T_{c1}$ and $T_{c2}$, exhibit common temperature ranges for P4 and P5. Sharp, high-intensity peaks indicated a fast crystallisation process, typically related to amorphous phase separation and nucleation. Fast events have also been related to the morphology (dimensionality) of the crystals forming [71], with the kinetics of the formation of two-dimensional crystals (plates) being faster than those of one-dimensional (needle-shaped) and three-dimensional crystals (cubic and spherical particles) [71]. Shape, intensity and end point of the crystallisation peaks are also affected by the direction of the crystal growth fronts [71]. For example, crystallisation of plate-like particles results in a higher intensity peak, due to an initially larger crystallising surface. It also drops more abruptly when

the crystal growth fronts perpendicular to its larger faces meet in the particle centre than those observed for spherical or cubic particles [71]. For P5, the first and very narrow crystallisation peak is therefore attributed to fluorapatite crystallisation (pine leaf-shaped crystals), while cuspidine and xonotlite crystallisation are probably included in the second crystallisation peak.

The Johnson-Mehl-Avrami-Kolmogorov (JMAK) [72] and Kissinger equations [73] for the interpretation of crystallisation behaviour are only valid if both the Avrami parameter *n* and the activation energy for crystallisation remain constant over the entire crystallisation process [71], [72], [74]. In the present study, a variation in activation energy (E) with crystallisation degree, *x*, and heating rate is expected from the diversity of crystalline phases. Thus, the use of the JMAK equation seems inappropriate, especially as it is also limited to non-isothermal crystallisation studies [71], [72], [75]. The Kissinger equation cannot be used either, as it is limited to surface crystallisation, while the narrow crystallisation peaks of P4 and P5 suggest bulk crystallisation. Therefore, E of glasses P0, P4 and P5 was determined by an iso-conversional method following Friedman's equation (Eq. 2) [74], [76], [77], [78], [79], [80].

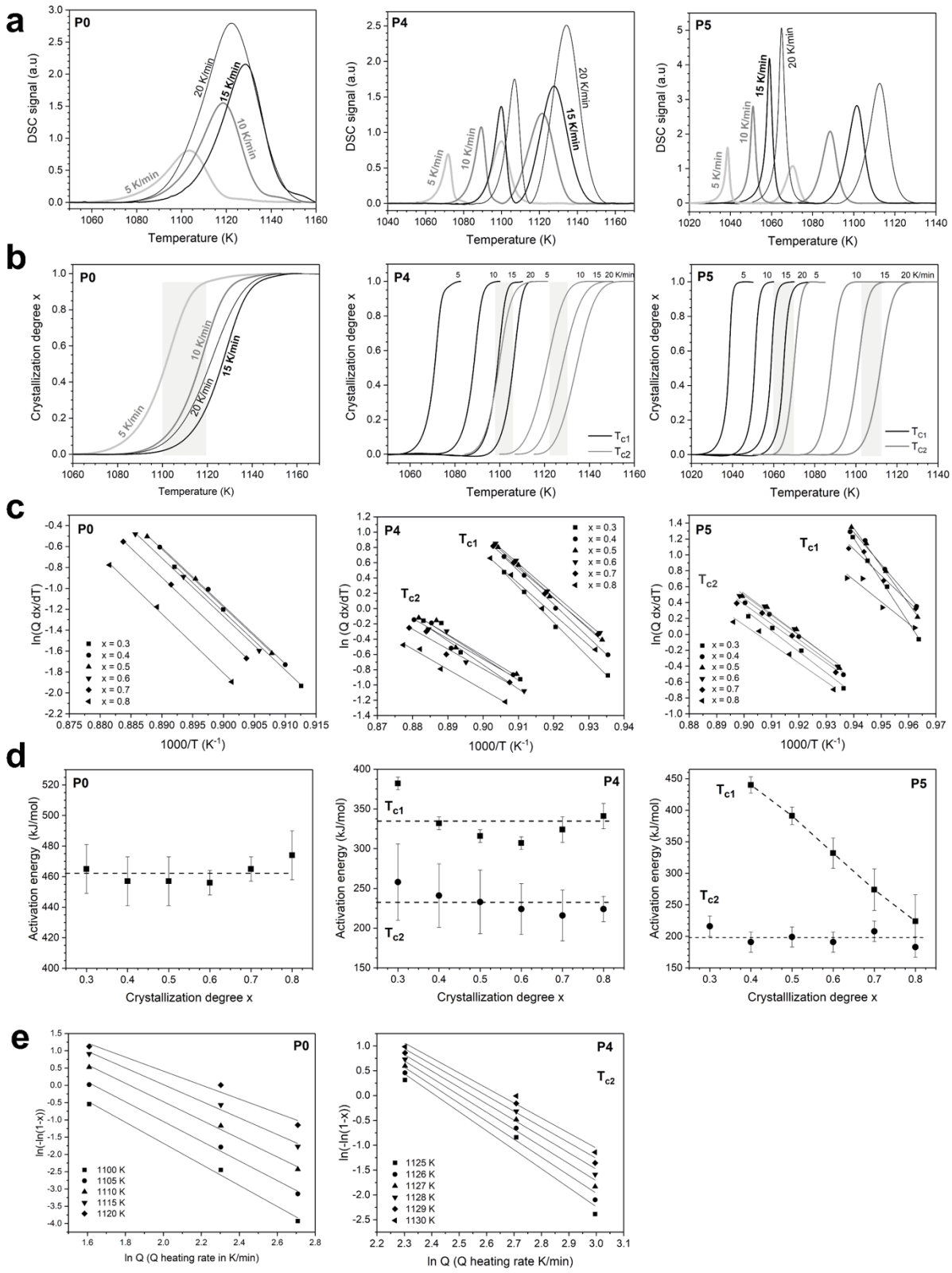


***Figure 7.*** *(a) DSC curves showing the crystallisation peaks for glasses P0, P4 and P5 at heating rates from 5 to 20 K/min. (b) Crystallisation degree, x, as a function of temperature. (c) Friedman's plot for calculating the activation energy according to the iso-conversional method. (d) Activation energy as a function of crystallisation degree. (e) Ozawa plot for calculating the Avrami parameter for P0 and P4.*

$$ln\left(\frac{dx}{dt}\right) = ln\left(Q\frac{dx}{dT}\right) = -\frac{E}{RT} + constant \quad (2)$$

Here, Q is the heating rate, *x* the crystallisation degree and *dx/dt* the rate of transformation at temperature T. The activation energy, E, was taken from the average of the $E_i$ values collected from the plot of *ln*(Q d(x)/dT) *vs.* 1000/T (Figure 7c). For P4 and P5, both crystallisation peaks were investigated. For glass P0, the curve at 20 K/min was excluded because of its unusual shift compared to the curves obtained at lower heating rates. Figure 7d displays E as a function of crystallisation degree, *x*. For glass P0, E is constant within the error limits (462±13 kJ/mol).

When applying Eq. 2 to both crystallisation peaks of glass P5 (Figure 7c), E of $T_{c1}$ decreased with progressing crystallisation (Figure 7d) from 440±13 kJ/mol at 40% crystallisation (x = 0.4) to 224±42 kJ/mol at 80%. This change of E over the crystallisation degree for $T_{c1}$ may indicate crystallisation of fluorapatite involving more than one step, probably including both surface and volume crystallisation. But it may also reflect a compositional change of the residual glassy matrix over the course of crystallisation. In contrast to $T_{c1}$, E of the second crystallisation peak, $T_{c2}$, of P5 remained nearly constant (198±16 kJ/mol) through the entire transformation. This value is lower than even the lowest one obtained for $T_{c1}$ (224 kJ/mol at *x* = 0.8, Figure 7d), suggesting that the crystallisation of cuspidine and xonotlite presents a lower energetic barrier than fluorapatite in glass P5. The lower values of E for P5 compared to phosphate-free glass P0 further confirmes the role of phosphate in nucleation and crystallisation, in good agreement with the Hrubý parameter, $K_H$ (Figure 1). Pinckney et al. [41] also reported on a change in nucleation/crystallisation mechanism from bulk to surface-dominated once the $P_2O_5$ content was increased to above 5 wt%, caused by a suppression of $CaF_2$-driven phase separation by phosphate-driven phase separation.

For glass P4, only the curves at higher heating rates show some overlap (Figure 7a,b), similar to P5. However, similar to P0, E of both crystallisation peaks for P4 remained constant within the error limits at 334±11kJ/mol for $T_{c1}$ and at 232±35kJ/mol for $T_{c2}$ (Figure 7d). While for P5 the contribution of both surface and bulk crystallisation of fluorapatite ($T_{c1}$) decreased the activation energy over the course of the process, fluorapatite crystallisation in P4 ($T_{c1}$) followed a simpler mechanism with a constant activation energy. E for $T_{c2}$ is similar for P4 and P5, in agreement cuspidine and xonotlite crystallisation in this temperature range (Figure 2c).

A further question to be looked into was whether E and $K_H$ (stability against crystallisation, Figure 1) correlated. P5, having the lowest value of $K_H$, showed the lowest values of E. By contrast, $K_H$ values of P4 and P0 were similar but their E values were not. This agrees with reports in the literature that a correlation between E and $K_H$ (or other glass stability parameters) is not always possible [81], [82]. The fact that the glasses studied here showed phase separation (as reported previously [34]) probably plays a role, as phase separation droplets may act as nuclei either by shifting the composition of one of the two glassy phases closer to that of the crystalline phase or by providing internal surfaces for heterogenous nucleation [83]. This means that the crystallisation process is dominated by crystal growth, with nucleation not having a pronounced influence. The crystal growth component in the studied samples is challenging to interpret, since the observed crystals seem to be composed of needles (one-dimensional), plates (two-dimensional) and additional three-dimensional crystals (Figures 4 to 6), with the dimensionality of the crystals altering the activation energy of crystallisation.

The Avrami exponent, *n*, provides information on the nature of the crystallisation mechanism. The classical Ozawa plot [71] was used to determine *n* in crystallisation events showing a constant value of E over the entire process, P0 and P4/$T_{c2}$ (Table 4). For P0, the Avrami parameter decreased from 3 at lower temperatures to 2 at higher temperatures, indicating that, despite E being constant, *n* changed with crystallisation degree. Changes of *n*

have been reported for other glass systems as a function of particle size [84] or temperature [85]. Since the broad crystallisation peak of glass P0 includes the crystallisation of xonotlite, cuspidine and wollastonite, the global value of *n* may change depending on the crystallisation mechanism and crystal morphology of these phases. According to Donald [86], a constant value of E and *n* = 2 or 3 would indicate a two- or three-dimensional volume crystallisation mechanism with a constant number of nuclei (well nucleated sample with number of nuclei being independent from the heating rate), which agrees with the initial phase separation observed in the present glass system [34] and with the radiating and needle-like microstructures observed for P0-846 (Figure 4). In order to validate the values of *n*, the Augis-Bennett equation [87] (Eq. 3) was used to determine the Avrami parameter when E is known:

$$n = \frac{2.5}{FWHM}\frac{RT_c^2}{E} \quad (3)$$

Here R is the gas constant and FWHM is the full width at half maximum of the DSC crystallisation peak at temperature $T_c$. Table 4 shows the *n* values calculated for each crystallisation peak as a function of the heating rate. Using Eq. 3 and E = 462 kJ/mol, the mean value of *n* for the overall crystallisation process is 2.5, agreeing with the *n* values obtained by the Ozawa plot varying between 2 and 3.

***Table 4.*** *Avrami parameters of glasses P0 and P4 determined from the Ozawa plot [71] and the Augis-Bennett equation [87] (Eq. 3).*

| **P0** | | | | | | | |
|---|---|---|---|---|---|---|---|
| **Ozawa** | T (K) | 1100 | 1105 | 1110 | 1115 | 1120 | |
| | *n* | 3.0 ± 0.2 ($R^2$ = 0.994) | 2.7 ± 0.2 ($R^2$ = 0.995) | 2.8 ± 0.2 ($R^2$ = 0.996) | 2.4 ± 0.2 ($R^2$ = 0.992) | 2.0 ± 0.3 ($R^2$ = 0.97) | |
| **Augis-Bennett** | Q (K/min) | 5 | 10 | 15 | 20 | | |
| (E = 462 kJ/mol) | *n* | 2.6 | 2.7 | 2.7 | 2.0 | | |
| **P4-$T_{c2}$** | | | | | | | |
| **Ozawa** | T (K) | 1125 | 1126 | 1127 | 1128 | 1129 | 1130 |
| | *n* | 3.8 ± 0.2 ($R^2$ = 0.97) | 3.6 ± 0.6 ($R^2$ = 0.97) | 3.4 ± 0.6 ($R^2$ = 0.97) | 3.3 ± 0.5 ($R^2$ = 0.98) | 3.1 ± 0.5 ($R^2$ = 0.98) | 3.0 ± 0.4 ($R^2$ = 0.98) |

For P5, the reduced overlap of the crystallisation degree curves of the two crystallisation peaks (Figure 7b) leads to non-reliable *n* values calculated from the Ozawa plot, as only two *x* curves show an overlap, and the error associated with both large and small values of *x* (the tails of the x curve) would therefore be large. Moreover, for $T_{c1}$ (with its small FWHM of less than 3 K) with a constant E, the Avrami exponent determined by the Augis-Bennett equation (Eq. 3) delivered a value much larger than 4, which has no physical meaning. According to Augis-Bennett, the shape of the DSC peak determines the value of *n*, meaning that the narrower the peak, the larger is *n* [87]. Based on the work by Matusita et al. [88] plotting ln(- ln(1-x) as a function of 1/T provides insight in the crystallisation behaviour [78], [89]. Here, the plot of $T_{c1}$ of glass P5 (Figure 8) is clearly non-linear, indicating the complex nature of the crystallisation process, involving different stages (i.e., different *n* values). The loss of linearity in this plot has been associated with the saturation of the nucleation sites of the final crystallisation stage [78]. The same was found for $T_{c2}$ of P5, due to the narrow overlap of the crystallisation degree curves and a very small FWHM. This finding agrees with surface and

volume crystallisation of fluorapatite ($T_{c1}$) and the nearly parallel crystallisation of cuspidine and xonotlite ($T_{c2}$).

For $T_{c1}$ of glass P4, associated with the crystallisation of fluorapatite, only the crystallisation degree curves of 15 and 20 K/min overlap in a narrow temperature range, making a determination of the Avrami exponent *n* impossible, as explained above. Determination of *n* through the Augis-Bennett equation is not reliable either. For $T_{c2}$, the crystallisation degree curves at 10, 15 and 20 K/min overlap in a certain temperature range, enabling the determination of *n* through the Ozawa plot between 1125 and 1130 K (Figure 7e, Table 4). A mean value of *n* = 3 was obtained. Again, the narrow shape of the $T_{c2}$ peak, being less than 20 K, did not allow for an additional calculation of *n* through the Augis-Bennett equation. For $T_{c2}$ with its constant E, *n* = 3 indicates three-dimensional volume crystallisation (of cuspidine, xonotlite and wollastonite) with a constant number of nuclei (well nucleated sample with number of nuclei being independent on the heating rate) [86].

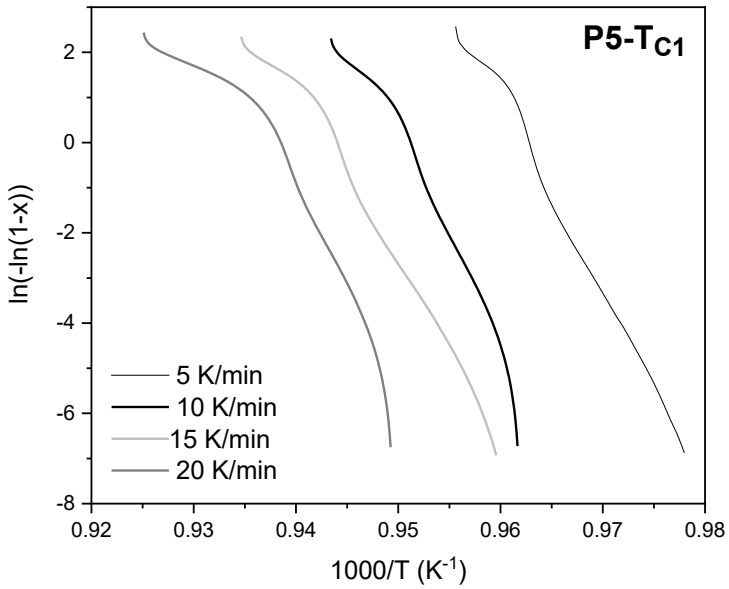


***Figure 8.*** *Representation of ln(−ln (1−α)) versus 1000/T at different heating rates for the first crystallisation peak $T_{c1}$ of glass P5. The plot is clearly non-linear, indicating the complex nature of the crystallisation process.*

Taken together, the crystallisation mechanism varies as a function of the phosphate to silicate ratio. A volume crystallisation mechanism with a constant activation energy over the whole crystallisation process was observed for phosphate-free glass P0, while for P5 contributions of both surface and volume crystallisation of fluorapatite need to be considered. Here, the activation energy strongly decreased during crystallisation due to increasing contributions of surface crystallisation at the expense of volume crystallisation. At the second crystallisation temperature (assigned to silicate phases), crystallisation followed an internal process with a constant activation energy. For glass P4, fluorapatite crystallisation was less complex than for P5, showing a constant E, probably only including surface crystallisation. The crystallisation of silicate phases occurred in a similar way in P4 and P5.

## 4. Conclusions

This work highlights the possibility to tailor the crystal phases and crystalline fractions as a function of phosphate to silicate ratio in bioactive glasses. The presence of fluorapatite is beneficial as it potentially facilitates apatite surface precipitation in contact with physiological

solutions. On the other hand, wollastonite is known to improve the mechanical properties. This work shows that by changing the phosphate to silicate ratio we can obtain fluorapatite-free or wollastonite-free glass-ceramics, which potentially allows for the properties to be tuned to best suit the final application. It remains to be investigated how these changes in crystal phases affect the reactions of the glasses in contact with physiological solutions, especially in comparison with the parent glasses. This will be the subject of future studies.

## Data availability statement

Data are available from the corresponding authors upon request.

## Underlying and related material

A supplementary video of *in situ* high temperature optical microscopy of a bulk sample of glass P0 at 846°C is available online: DOI: 10.5281/zenodo.10730637.

## Author contributions

DSB and JM: conceptualisation, funding acquisition, supervision; GK, JMSS, NK, RGH and APM: formal analysis; ATCJ, GK, CP, JMSS, NK and APM: investigation, visualisation; ATCJ, GK and APM: writing – original draft; all authors: writing – review & editing.

## Competing interests

The authors declare no competing interests.

## Funding

The authors acknowledge funding by the German Research Foundation (DFG; grant numbers BR 4608/7-1, PA 3095/1-1 and WE 4051/21-1) as well as by the German Academic Exchange Service and the Academy of Finland for a bilateral exchange programme.

## Acknowledgement

The authors would like to thank Steffi Ebbinghaus, Gabi Möller, Lutz Preißer and Thomas Kittel (Otto Schott Institute, Jena) for XRD measurements, sample preparation and *in situ* heating microscopy analysis, respectively. The authors also thank Dr Harold Toms (Queen Mary University of London) for assistance with NMR experiments and Andrea Böbenroth (Fraunhofer IMWS) for optical microscopy imaging.

## References

[1] D. S. Brauer, "Bioactive glasses—structure and properties," *Angew Chem Int Edit,* vol. 54, no. 14, pp. 4160-4181, 2015, doi: 10.1002/anie.201405310.

[2] O. Guillon, S. Y. Cao, J. Y. Chang, L. Wondraczek, and A. R. Boccaccini, "Effect of uniaxial load on the sintering behaviour of 45S5 Bioglass® powder compacts," (in English), *J Eur Ceram Soc,* vol. 31, no. 6, pp. 999-1007, Jun 2011, doi: 10.1016/J.Jeurceramsoc.2010.12.031.

[3] C. Blaeß, R. Müller, G. Poologasundarampillai, and D. S. Brauer, "Sintering and concomitant crystallisation of bioactive glasses," *Int J Appl Glass Sci,* vol. 10, no. 4, pp. 449-462, 2019, doi: 10.1111/ijag.13477.

[4] A. R. Boccaccini, Q. Chen, L. Lefebvre, L. Gremillard, and J. Chevalier, "Sintering, crystallisation and biodegradation behaviour of Bioglass®-derived glass-ceramics," *Faraday Discuss,* 10.1039/B616539G vol. 136, no. 0, pp. 27-44, 2007, doi: 10.1039/b616539g.

[5] O. Peitl Filho, G. P. LaTorre, and L. L. Hench, "Effect of crystallization on apatite-layer formation of bioactive glass 45S5," (in English), *J Biomed Mater Res,* vol. 30, no. 4, pp. 509-514, Apr 1996. [Online]. Available: <Go to ISI>://WOS:A1996UD18300011.

[6] T. Duminis, S. Shahid, and R. G. Hill, "Apatite glass-ceramics: A review," (in English), *Frontiers in Materials,* vol. 3, Jan 9 2017, doi: 10.3389/fmats.2016.00059.

[7] W. Höland *et al.*, "Control of phase formation processes in glass-ceramics for medicine and technology," *J Non-Cryst Solids,* vol. 129, no. 1-3, pp. 152-162, Mar 1991, doi: 10.1016/0022-3093(91)90091-j.

[8] O. Peitl Filho, E. D. Zanotto, and L. L. Hench, "Highly bioactive $P_2O_5$-$Na_2O$-CaO-$SiO_2$ glass-ceramics," *J Non-Cryst Solids,* vol. 292, no. 1-3, pp. 115-126, 2001 2001. [Online]. Available: <Go to ISI>://000171993300011.

[9] I. Kansal *et al.*, "Diopside ($CaO{\cdot}MgO{\cdot}2SiO_2$)–fluorapatite ($9CaO{\cdot}3P_2O_5{\cdot}CaF_2$) glass-ceramics: potential materials for bone tissue engineering," *J. Mater. Chem.,* 10.1039/C1JM11876E vol. 21, no. 40, pp. 16247-16256, 2011, doi: 10.1039/C1JM11876E.

[10] A. Motealleh, S. Eqtesadi, A. Civantos, A. Pajares, and P. Miranda, "Robocast 45S5 bioglass scaffolds: in vitro behavior," *J. Mater. Sci,* vol. 52, no. 15, pp. 9179-9191, 2017/08/01 2017, doi: 10.1007/s10853-017-0775-5.

[11] M. A. Sainz, P. Pena, S. Serena, and A. Caballero, "Influence of design on bioactivity of novel $CaSiO_3$-$CaMg(SiO_3)_2$ bioceramics: In vitro simulated body fluid test and thermodynamic simulation," *Acta Biomater.,* Article vol. 6, no. 7, pp. 2797-2807, 2010, doi: 10.1016/j.actbio.2010.01.003.

[12] T. Kokubo, "Bioactive glass ceramics: properties and applications," *Biomaterials,* vol. 12, no. 2, pp. 155-163, 1991/03/01/ 1991, doi: 10.1016/0142-9612(91)90194-F.

[13] H. Oonishi *et al.*, "Quantitative comparison of bone growth behavior in granules of Bioglass®, A-W glass-ceramic, and hydroxyapatite," *J Biomed Mater Res,* vol. 51, no. 1, pp. 37-46, 2000, doi: 10.1002/(sici)1097-4636(200007)51:1<37::aid-jbm6>3.0.co;2-t.

[14] H. R. Fernandes, A. Gaddam, A. Rebelo, D. Brazete, G. E. Stan, and J. M. F. Ferreira, "Bioactive glasses and glass-ceramics for healthcare applications in bone regeneration and tissue engineering," (in eng), *Materials,* vol. 11, no. 12, p. 2530, Dec 12 2018, doi: 10.3390/ma11122530.

[15] J. K. M. F. Daguano, S. O. Rogero, M. C. Crovace, O. Peitl, K. Strecker, and C. Dos Santos, "Bioactivity and cytotoxicity of glass and glass-ceramics based on the 3CaO-$P_2O_5$-$SiO_2$-MgO system," *J. Mater. Sci. Mater. Med.,* Article vol. 24, no. 9, pp. 2171-2180, 2013, doi: 10.1007/s10856-013-4972-8.

[16] C. Ritzberger, M. Schweiger, and W. Höland, "Principles of crystal phase formation in Ivoclar Vivadent glass-ceramics for dental restorations," *J. Non-Cryst. Solids,* vol. 432, pp. 137-142, 2016/01/15/ 2016, doi: 10.1016/j.jnoncrysol.2015.04.034.

[17] X. Chen, X. Chen, D. S. Brauer, R. M. Wilson, R. G. Hill, and N. Karpukhina, "Bioactivity of sodium free fluoride containing glasses and glass-ceramics," *Materials,* vol. 7, no. 8, pp. 5470-5487, 2014, doi: 10.3390/ma7085470.

[18] W. Höland, V. Rheinberger, and M. Frank, "Mechanisms of nucleation and controlled crystallization of needle-like apatite in glass-ceramics of the $SiO_2$-$Al_2O_3$-$K_2O$-CaO-$P_2O_5$ system," *J. Non-Cryst. Solids,* vol. 253, pp. 170-177, 1999, doi: 10.1016/S0022-3093(99)00351-8.

[19] W. Höland, V. Rheinberger, S. Wegner, and M. Frank, "Needle-like apatite-leucite glass-ceramic as a base material for the veneering of metal restorations in dentistry,"

(in English), *J. Mater. Sci. Mater. Med.,* vol. 11, no. 1, pp. 11-17, Jan 2000. [Online]. Available: <Go to ISI>://WOS:000084253000002.

[20] W. Höland *et al.*, "Formation and crystal growth of needle-like fluoroapatite in functional glass-ceramics," *J. Mater. Chem.,* 10.1039/B714913A vol. 18, no. 12, pp. 1318-1332, 2008, doi: 10.1039/B714913A.

[21] R. Müller, L. A. Abu-Hilal, S. Reinsch, and W. Höland, "Coarsening of needle-shaped apatite crystals in $SiO_2$ • $Al_2O_3$ • $Na_2O$ • $K_2O$ • CaO • $P_2O_5$ • F glass," *J. Mater. Sci,* vol. 34, no. 1, pp. 65-69, 1999/01/01 1999, doi: 10.1023/A:1004457305970.

[22] D. S. Brauer, R. G. Hill, and M. D. O'Donnell, "Crystallisation of fluoride-containing bioactive glasses," *Phys Chem Glasses,* vol. 53, no. 2, pp. 27-30, 2012.

[23] M. W. G. Lockyer, D. Holland, and R. Dupree, "NMR investigation of the structure of some bioactive and related glasses," *J Non-Cryst Solids,* vol. 188, no. 3, pp. 207-219, 1995 1995, doi: 10.1016/0022-3093(95)00188-3.

[24] A. Pedone, T. Charpentier, G. Malavasi, and M. C. Menziani, "New insights into the atomic structure of 45S5 bioglass by means of solid-state NMR spectroscopy and accurate first-principles simulations," *Chem Mater,* vol. 22, no. 19, pp. 5644-5652, 2010 2010, doi: 10.1021/cm102089c.

[25] G. Kirste *et al.*, "Bioactive glass-ceramics containing fluorapatite, xonotlite, cuspidine and wollastonite form apatite faster than their corresponding glasses," *Sci Rep,* vol. 14, no. 1, p. 3997, Feb 18 2024, doi: 10.1038/s41598-024-54228-0.

[26] M. D. O'Donnell, S. J. Watts, R. G. Hill, and R. V. Law, "The effect of phosphate content on the bioactivity of soda-lime-phosphosilicate glasses," *J Mater Sci-Mater M,* vol. 20, no. 8, pp. 1611-1618, 2009 2009, doi: 10.1007/s10856-009-3732-2.

[27] R. G. Hill and D. S. Brauer, "Predicting the bioactivity of glasses using the network connectivity or split network models," *J Non-Cryst Solids,* vol. 357, no. 24, pp. 3884-3887, 2011 2011, doi: 10.1016/j.jnoncrysol.2011.07.025.

[28] A. Calver, R. G. Hill, and A. Stamboulis, "Influence of fluorine content on the crystallization behavior of apatite-wollastonite glass-ceramics," *J Mater Sci,* vol. 39, no. 7, pp. 2601-2603, 2004/04/01 2004, doi: 10.1023/B:JMSC.0000020038.79675.0f.

[29] J. F. Stebbins and Q. Zeng, "Cation ordering at fluoride sites in silicate glasses: a high-resolution $^{19}F$ NMR study," *J Non-Cryst Solids,* vol. 262, no. 1-3, pp. 1-5, 2000 2000. [Online]. Available: WOS:000085311800001.

[30] T. Höche, J. W. Gerlach, and T. Petsch, "Static-charging mitigation and contamination avoidance by selective carbon coating of TEM samples," *Ultramicroscopy,* vol. 106, no. 11, pp. 981-985, 2006/10/01/ 2006, doi: 10.1016/j.ultramic.2006.05.007.

[31] A. A. Cabral Jr, C. Fredericci, and E. D. Zanotto, "A test of the Hruby parameter to estimate glass forming ability," *J. Non-Cryst. Solids,* vol. 219, pp. 182-186, 10/01 1997, doi: 10.1016/S0022-3093(97)00327-X.

[32] J. Jiusti, D. R. Cassar, and E. D. Zanotto, "Which glass stability parameters can assess the glass-forming ability of oxide systems?," *Int J. Appl. Glass Sci.,* vol. 11, no. 4, pp. 612-621, 2020, doi: 10.1111/ijag.15416.

[33] A. Tilocca and A. N. Cormack, "Structural effects of phosphorus inclusion in bioactive silicate glasses," *J Phys Chem B,* vol. 111, no. 51, pp. 14256-14264, 2007 2007, doi: 10.1021/jp075677o.

[34] A. T. Contreras Jaimes *et al.*, "Nano-imaging confirms improved apatite precipitation for high phosphate/silicate ratio bioactive glasses," *Sci Rep,* vol. 11, no. 1, p. 19464, 2021/09/30 2021, doi: 10.1038/s41598-021-98863-3.

[35] X. Chatzistavrou, T. Zorba, E. Kontonasaki, K. Chrissafis, P. Koidis, and K. M. Paraskevopoulos, "Following bioactive glass behavior beyond melting temperature by thermal and optical methods," *Phys. Status Solidi A,* vol. 201, no. 5, pp. 944-951, 2004, doi: 10.1002/pssa.200306776.

[36] D. Groh, F. Döhler, and D. S. Brauer, "Bioactive glasses with improved processing. Part 1. Thermal properties, ion release and apatite formation," *Acta Biomater,* vol. 10, no. 10, pp. 4465–4473, 2014, doi: 10.1016/j.actbio.2014.05.019.

[37] Ö. H. Andersson, "Glass transition temperature of glasses in the $SiO_2$-$Na_2O$-CaO-$P_2O_5$-$Al_2O_3$-$B_2O_3$ System," *J Mater Sci-Mater M,* vol. 3, no. 5, pp. 326-328, 1992 1992. [Online]. Available: WOS:A1992JP86100003.

[38] T. Watanabe, H. Fukuyama, and K. Nagata, "Stability of cuspidine ($3CaO$-$2SiO_2$-$CaF_2$) and phase relations in the CaO-$SiO_2$-$CaF_2$ system," (in English), *ISIJ International,* vol. 42, no. 5, pp. 489-497, 2002, doi: 10.2355/isijinternational.42.489.

[39] I. Kansal, D. U. Tulyaganov, A. Goel, M. J. Pascual, and J. M. F. Ferreira, "Structural analysis and thermal behavior of diopside–fluorapatite–wollastonite-based glasses and glass–ceramics," *Acta Biomater.,* vol. 6, no. 11, pp. 4380-4388, 2010/11/01/ 2010, doi: 10.1016/j.actbio.2010.05.019.

[40] X. J. Chen, N. Karpukhina, D. S. Brauer, and R. G. Hill, "High chloride content calcium silicate glasses," (in English), *Phys Chem Chem Phys,* vol. 19, no. 10, pp. 7078-7085, Mar 14 2017, doi: 10.1039/c6cp07905a.

[41] L. R. Pinckney, G. H. Beall, and R. L. Andrus, "Strong sintered miserite glass-ceramics," *J. Am. Ceram. Soc.,* vol. 82, no. 9, pp. 2523-2528, 1999, doi: 10.1111/j.1151-2916.1999.tb02114.x.

[42] N. Kanchanarat, C. A. Miller, P. V. Hatton, P. F. James, and I. M. Reaney, "Early stages of crystallization in canasite-based glass ceramics," *J. Am. Ceram. Soc.,* vol. 88, no. 11, pp. 3198-3204, 2005, doi: 10.1111/j.1551-2916.2005.00589.x.

[43] N. Y. Mostafa, A. A. Shaltout, H. Omar, and S. A. Abo El-Enein, "Hydrothermal synthesis and characterization of aluminium and sulfate substituted 1.1nm tobermorites," *J. Alloys Compd.,* vol. 467, no. 1, pp. 332-337, 2009/01/07/ 2009, doi: 10.1016/j.jallcom.2007.11.130.

[44] E. John, C. Lehmann, and D. Stephan, "Xonotlite and hillebrandite as model compounds for calcium silicate hydrate seeding in cementitious materials," *Transportation Research Record,* vol. 2675, no. 9, pp. 65-72, 2021, doi: 10.1177/0361198120943205.

[45] L. Grund Bäck, S. Ali, S. Karlsson, D. Moncke, E. I. Kamitsos, and B. Jonson, "Mixed alkali/alkaline earth-silicate glasses: Physical properties and structure by vibrational spectroscopy," (in English), *Int J Appl Glass Sci,* vol. 10, no. 3, pp. 349-362, Jul 2019, doi: 10.1111/ijag.13101.

[46] A. de Pablos-Martín, A. T. Contreras Jaimes, S. Wahl, S. Meyer, and D. S. Brauer, "Fluorine loss determination in bioactive glasses by laser-induced breakdown spectroscopy (LIBS)," *Int J Appl Glass Sci,* vol. 12, no. 2, pp. 213-221, 2021, doi: 10.1111/ijag.15867.

[47] M. T. Hamedani, V. K. Marghussian, and H. Sarpoolaky, "Effect of composition and heat treatment on the phase evolution and mechanical properties of tough miserite-based glass ceramics," *J. Non-Cryst. Solids,* vol. 382, pp. 112-120, 2013/12/15/ 2013, doi: 10.1016/j.jnoncrysol.2013.10.015.

[48] R. Levinskas *et al.*, "Modified xonotlite–type calcium silicate hydrate slabs for fire doors," *J. Fire Sci.,* vol. 36, no. 2, pp. 83-96, 2018, doi: 10.1177/0734904118754381.

[49] N. Karpukhina, R. G. Hill, and R. V. Law, "Crystallisation in oxide glasses - a tutorial review," *Chemical Society Reviews,* 10.1039/C3CS60305A vol. 43, no. 7, pp. 2174-2186, 2014, doi: 10.1039/c3cs60305a.

[50] M. Jarlbring, D. E. Sandström, O. N. Antzutkin, and W. Forsling, "Characterization of active phosphorus surface sites at synthetic carbonate-free fluorapatite using single-pulse H-1, P-31, and T-31 CP MAS NMR," (in English), *Langmuir,* vol. 22, no. 10, pp. 4787-4792, May 9 2006, doi: 10.1021/la052837j.

[51] F. M. McCubbin *et al.*, "Synthesis and characterization of low-$OH^-$ fluor-chlorapatite: A single-crystal XRD and NMR spectroscopic study," (in English), *Am Mineral,* vol. 93, no. 1, pp. 210-216, Jan 2008, doi: 10.2138/am.2008.2557.

[52] X. Chen, X. Chen, D. S. Brauer, R. M. Wilson, R. G. Hill, and N. Karpukhina, "Novel alkali free bioactive fluorapatite glass ceramics," *J Non-Cryst Solids,* vol. 402, pp. 172-177, 2014, doi: 10.1016/j.jnoncrysol.2014.05.025.

[53] I. Elgayar, A. E. Aliev, A. R. Boccaccini, and R. G. Hill, "Structural analysis of bioactive glasses," *J Non-Cryst Solids,* vol. 351, no. 2, pp. 173-183, 2005 2005, doi: 10.1016/j.jnoncrysol.2004.07.067.

[54] C. Jäger, T. Welzel, W. Meyer-Zaika, and M. Epple, "A solid-state NMR investigation of the structure of nanocrystalline hydroxyapatite," *Magn. Reson. Chem.,* vol. 44, no. 6, pp. 573-580, 2006, doi: 10.1002/mrc.1774.

[55] Y. J. Gao, N. Karpukhina, and R. V. Law, "Phase segregation in hydroxyfluorapatite solid solution at high temperatures studied by combined XRD/solid state NMR," (in English), *RSC Adv,* vol. 6, no. 105, pp. 103782-103790, 2016, doi: 10.1039/c6ra17161c.

[56] M. Braun, P. Hartmann, and C. Jana, "$^{19}$F and $^{31}$P NMR spectroscopy of calcium apatites," *J. Mater. Sci. Mater. Med.,* vol. 6, no. 3, pp. 150-154, 1995/03/01 1995, doi: 10.1007/BF00120291.

[57] D. S. Brauer, N. Karpukhina, M. D. O'Donnell, R. V. Law, and R. G. Hill, "Fluoride-containing bioactive glasses: Effect of glass design and structure on degradation, pH and apatite formation in simulated body fluid," *Acta Biomater,* vol. 6, pp. 3275-3282, 2010 2010, doi: 10.1016/j.actbio.2010.01.043.

[58] A. Stamboulis, R. G. Hill, R. V. Law, and S. Matsuya, "A MAS NMR study of the crystallisation process of apatite-mullite glass-ceramics," *Key Engineering Materials,* vol. 254-256, pp. 99-102, 2004. [Online]. Available: https://www.scientific.net/KEM.254-256.99.

[59] R. G. Hill, N. Da Costa, and R. V. Law, "Characterization of a mould flux glass," *J Non-Cryst Solids,* vol. 351, no. 1, pp. 69-74, 2005 2005. [Online]. Available: <Go to ISI>://000226273200010.

[60] R. G. Hill *et al.*, "Characterisation of fluorine containing glasses and glass-ceramics by F-19 magic angle spinning nuclear magnetic resonance spectroscopy," *J Eur Ceram Soc,* vol. 29, no. 11, pp. 2185-2191, 2009 2009. [Online]. Available: WOS:000267394700007.

[61] F. Munoz *et al.*, "NMR investigation of the crystallization mechanism of $LaF_3$ and $NaLaF_4$ phases in aluminosilicate glasses," (in English), *J. Non-Cryst. Solids,* vol. 357, no. 5, pp. 1463-1468, Mar 1 2011, doi: 10.1016/j.jnoncrysol.2010.11.024.

[62] O. A. Al-Harbi and E. M. A. Hamzawy, "Stable wollastonite-cuspidine glass-ceramic using inexpensive raw materials," *Silicon,* vol. 6, no. 4, pp. 257-264, 2014/10/01 2014, doi: 10.1007/s12633-014-9241-z.

[63] T. Watanabe, H. Hashimoto, M. Hayashi, and K. Nagata, "Effect of alkali oxides on crystallization in $CaO$-$SiO_2$-$CaF_2$ glasses," *ISIJ Int.,* vol. 48, no. 7, pp. 925-933, 2008, doi: 10.2355/isijinternational.48.925.

[64] J. Yang and M. Zhu, "Evolution of compositions and properties of $CaO–SiO_2$ based mold flux for continuous casting high Mn Steel," *ISIJ Int.,* vol. 56, pp. 2191-2198, 12/15 2016, doi: 10.2355/isijinternational.ISIJINT-2016-315.

[65] A. R. Hanifi, A. Genson, W. Redington, M. J. Pomeroy, and S. Hampshire, "Effects of nitrogen and fluorine on crystallisation of Ca–Si–Al–O–N–F glasses," *J. Eur. Ceram. Soc.,* vol. 32, no. 4, pp. 849-857, 2012/04/01/ 2012, doi: 10.1016/j.jeurceramsoc.2011.10.026.

[66] C. A. Miller, I. M. Reaney, P. V. Hatton, and P. F. James, "Crystallization of canasite/frankamenite-based glass-ceramics," (in English), *Chem. Mater.,* vol. 16, no. 26, pp. 5736-5743, Dec 28 2004, doi: 10.1021/cm048946l.

[67] C. C. Lin, K. S. Leung, P. Y. Shen, and S. F. Chen, "Elasticity and structure of the compounds in the wollastonite (CaSiO3)–Na2SiO3 system: from amorphous to crystalline state," *J. Mater. Sci. Mater. Med.,* vol. 26, no. 1, p. 39, 2015/01/15 2015, doi: 10.1007/s10856-014-5361-7.

[68] S. M. Salman, S. N. Salama, and H. A. Abo-Mosallam, "The crystallization behaviour and bioactivity of wollastonite glass-ceramic based on $Na_2O–K_2O–CaO–SiO_2–F$ glass system," *Journal of Asian Ceramic Societies,* vol. 3, no. 3, pp. 255-261, 2015, doi: 10.1016/j.jascer.2015.04.004.

[69] K. T. Stanton, K. P. O'Flynn, S. Kiernan, J. Menuge, and R. Hill, "Spherulitic crystallization of apatite-mullite glass-ceramics: Mechanisms of formation and implications for fracture properties," (in English), *J. Non-Cryst. Solids,* vol. 356, no. 35-36, pp. 1802-1813, Aug 1 2010. [Online]. Available: <Go to ISI>://WOS:000282395500010.

[70] T. Kokubo *et al.*, "Apatite and wollastonite-containing glass-ceramics for prosthetic application," *Bull. Inst. Chem. Res. Kyoto Univ.,* vol. 60, 01/01 1982.

[71] Q. J. Zheng *et al.*, "Understanding glass through differential scanning calorimetry," (in English), *Chem. Rev.,* vol. 119, no. 13, pp. 7848-7939, Jul 10 2019, doi: 10.1021/acs.chemrev.8b00510.

[72] M. Todinov, "On some limitations of the Johnson-Mehl-Avrami-Kolmogorov equation," *Acta Mater.,* vol. 48, 11/08 2000, doi: 10.1016/S1359-6454(00)00280-9.

[73] H. E. Kissinger, "Reaction kinetics in differential thermal analysis," *Anal Chem,* 1317-43-7 (Brucite); 13397-26-7 (Calcite); 13717-00-5 (Magnesite) (thermal analysis of) vol. 29, pp. 1702-1706, 1957 1957.

[74] A. Nommeots-Nomm *et al.*, "Phosphate/oxyfluorophosphate glass crystallization and its impact on dissolution and cytotoxicity," *Mater. Sci. Eng., C,* vol. 117, p. 111269, 2020/12/01/ 2020, doi: 10.1016/j.msec.2020.111269.

[75] I. Sinha and R. K. Mandal, "Avrami exponent under transient and heterogeneous nucleation transformation conditions," *J. Non-Cryst. Solids,* vol. 357, no. 3, pp. 919-925, 2011/02/01/ 2011, doi: 10.1016/j.jnoncrysol.2010.11.005.

[76] M. J. Starink, "The determination of activation energy from linear heating rate experiments: a comparison of the accuracy of isoconversion methods," *Thermochim. Acta,* vol. 404, no. 1, pp. 163-176, 2003/09/04/ 2003, doi: 10.1016/S0040-6031(03)00144-8.

[77] A. Ortega, "A simple and precise linear integral method for isoconversional data," *Thermochim. Acta,* vol. 474, no. 1, pp. 81-86, 2008/08/15/ 2008, doi: 10.1016/j.tca.2008.05.003.

[78] M. A. Abdel-Rahim, M. M. Hafiz, and A. Z. Mahmoud, "Crystallization kinetics of overlapping phases in $Se_{70}Te_{15}Sb_{15}$ using isoconversional methods," *Pro. Nat. Sci.-Mater,* vol. 25, no. 2, pp. 169-177, 2015/04/01/ 2015, doi: 10.1016/j.pnsc.2015.03.001.

[79] C. Dohare and N. Mehta, "Iso-conversional kinetic study of non-isothermal crystallization in glassy $Se_{98}Ag_2$ alloy," *J. Therm. Anal. Calorim.,* vol. 109, no. 1, pp. 247-253, 2012/07/01 2012, doi: 10.1007/s10973-011-1696-1.

[80] S. R. Teixeira, M. Romero, and J. M. Rincón, "Crystallization of $SiO_2$–CaO–$Na_2O$ glass using sugarcane bagasse ash as silica source," *J. Am. Ceram. Soc.,* vol. 93, no. 2, pp. 450-455, 2010, doi: 10.1111/j.1551-2916.2009.03431.x.

[81] K. K. Song, P. Gargarella, S. Pauly, G. Z. Ma, U. Kühn, and J. Eckert, "Correlation between glass-forming ability, thermal stability, and crystallization kinetics of Cu-Zr-Ag metallic glasses," *J. Appl. Phys.,* vol. 112, no. 6, p. 063503, 2012, doi: 10.1063/1.4752263.

[82] A. M. Rodrigues, L. D. Silva, R. Zhang, and V. O. Soares, "Structural effects on glass stability and crystallization," *CrystEngComm,* 10.1039/C7CE02135F vol. 20, no. 16, pp. 2278-2283, 2018, doi: 10.1039/C7CE02135F.

[83] E. D. Zanotto, "Effect of liquid phase separation on crystal nucleation in glass-formers. Case closed," (in English), *Ceram. Int.,* vol. 46, no. 16, pp. 24779-24791, Nov 2020, doi: 10.1016/j.ceramint.2020.06.305.

[84] A. Karamanov, I. Avramov, L. Arrizza, R. Pascova, and I. Gutzow, "Variation of Avrami parameter during non-isothermal surface crystallization of glass powders with different sizes," *J. Non-Cryst. Solids,* vol. 358, pp. 1486–1490, 07/01 2012, doi: 10.1016/j.jnoncrysol.2012.04.003.

[85] R. Wurth *et al.*, "Crystallisation mechanism of a multicomponent lithium alumino-silicate glass," *Mater. Chem. Phys.,* Article vol. 134, no. 2-3, pp. 1001-1006, 2012, doi: 10.1016/j.matchemphys.2012.03.103.

[86] I. Donald, "Crystallisation kinetics of a lithium zinc silicate glass studied by DTA and DSC," *J. Non-Cryst. Solids,* vol. 345, pp. 120-126, 10/01 2004, doi: 10.1016/j.jnoncrysol.2004.08.007.

[87] J. A. Augis and J. E. Bennett, "Calculation of the Avrami parameters for heterogeneous solid state reactions using a modification of the Kissinger method," *J. Therm. Anal.,* vol. 13, no. 2, pp. 283-292, 1978/04/01 1978, doi: 10.1007/BF01912301.

[88] K. Matusita, T. Komatsu, and R. Yokota, "Kinetics of non-isothermal crystallization process and activation energy for crystal growth in amorphous materials," *J. Mater. Sci,* vol. 19, no. 1, pp. 291-296, 1984/01/01 1984, doi: 10.1007/BF02403137.

[89] W. Lu, B. Yan, and W.-H. Huang, "Complex primary crystallization kinetics of amorphous Finemet alloy," *J. Non-Cryst. Solids,* vol. 351, no. 40, pp. 3320-3324, 2005/10/15/ 2005, doi: 10.1016/j.jnoncrysol.2005.08.018.